

Modeling the albedo of Earth-like magma ocean planets with H₂O-CO₂ atmospheres

W. Pluriel^{1,2}, E. Marcq², M. Turbet³

September 7, 2018

¹ Laboratoire d'astrophysique de Bordeaux, Univ. Bordeaux, CNRS, B18N, allée Geoffroy Saint-Hilaire, 33615 Pessac, France

² LATMOS/IPSL/CNRS/UPMC/UVSQ, Guyancourt, France

³ Laboratoire de Météorologie Dynamique, IPSL, Sorbonne Universités, UPMC Univ Paris 06, CNRS, 4 place Jussieu, 75005 Paris, France.

Abstract

During accretion, the young rocky planets are so hot that they become endowed with a magma ocean. From that moment, the mantle convective thermal flux control the cooling of the planet and an atmosphere is created by outgassing. This atmosphere will then play a key role during this cooling phase. Studying this cooling phase in details is a necessary step to explain the great diversity of the observed telluric planets and especially to assess the presence of surface liquid water. We used here a radiative-convective 1D atmospheric model (H₂O, CO₂) to study the impact of the Bond albedo on the evolution of magma ocean planets. We derived from this model the thermal emission spectrum and the spectral reflectance of these planets, from which we calculated their Bond albedos. Compared to [Marcq *et al.* \(2017\)](#), the model now includes a new module to compute the Rayleigh scattering, and state of the art CO₂ and H₂O gaseous opacities data in the visible and infrared spectral ranges. We show that the Bond albedo of these planets depends on their surface temperature and results from a competition between Rayleigh scattering from the gases and Mie scattering from the clouds. The colder the surface temperature is, the thicker the clouds are, and the higher the Bond albedo is. We also evidence that the relative abundances of CO₂ and H₂O in the atmosphere strongly impact the Bond albedo. The Bond albedo is higher for atmospheres dominated by the CO₂, better Rayleigh scatterer than H₂O. Finally, we provide the community with an empirical formula for the Bond albedo that could be useful for future studies of magma ocean planets.

Keywords: Atmospheres; albedo; spectroscopy; radiative transfer; modeling

1 Introduction

In order to better assess the history of the atmospheres of telluric planets, we need to better characterize the primitive atmospheres that these planets possessed at the very beginning of their history. These secondary atmospheres are outgassed during a relatively short stage lasting $10^5 \sim 10^6$ years ([Salvador *et al.*, 2017](#); [Lebrun *et al.*, 2013](#); [Hamano *et al.*, 2015](#)) named *magma ocean* (MO) stage.

The aim of this study is twofold: first, knowing the evolution of these atmospheres would better constrain the early habitability of a given telluric planet (defined here as the presence or not of liquid water on its surface) and second, the determination of the thermal emission spectrum and the spectral reflectance of atmospheres of MO planets would yield precious observational constraints upon MO exoplanets. In this context, several studies have already been made, generally using models coupled with various submodules (interior, atmosphere, escape) interacting with each other through matter and/or energy fluxes ([Hamano *et al.*, 2015](#); [Lupu *et al.*, 2014](#); [Lebrun *et al.*, 2013](#)). However, some of these models prescribe the albedo instead of computing it in a self-consistent way. Considering that albedo plays a major role in the thermal balance, and thus in the habitability and observable spectrum of such planets, the present study aims to improve its computation.

We will first describe the models used and the improvements made in Section 2, then we will present the results in Section 3 and finally we will discuss the limitations of our model and suggests some solutions in Section 4.

Spectral band [μm]	Spectral band [μm]
0.29-0.30	1.13-1.20
0.30-0.35	1.20-1.31
0.35-0.40	1.31-1.43
0.40-0.45	1.43-1.56
0.45-0.50	1.56-1.69
0.50-0.55	1.69-1.86
0.55-0.60	1.86-2.02
0.60-0.65	2.02-2.20
0.65-0.67	2.20-2.48
0.67-0.69	2.48-2.66
0.69-0.75	2.66-2.92
0.75-0.78	2.92-3.24
0.78-0.84	3.24-3.58
0.84-0.89	3.58-4.01
0.89-0.96	4.01-4.17
0.96-1.04	4.17-4.55
1.04-1.07	4.55-4.88
1.07-1.13	4.88-5.13

Table 1: List of the 36 thermal infrared spectral bands used in the model.

2 Model description

The atmospheric model used here, developed initially in [Marcq \(2012\)](#) and recently updated in [Marcq *et al.* \(2017\)](#), is a one-dimensional model extending from the surface up to an altitude corresponding to 0.1 Pa, taking into account radiative and convective processes in the atmosphere. The atmosphere, assumed here to be composed of H_2O and CO_2 , is divided into plane-parallel computational layers discretized according to pressure coordinates.

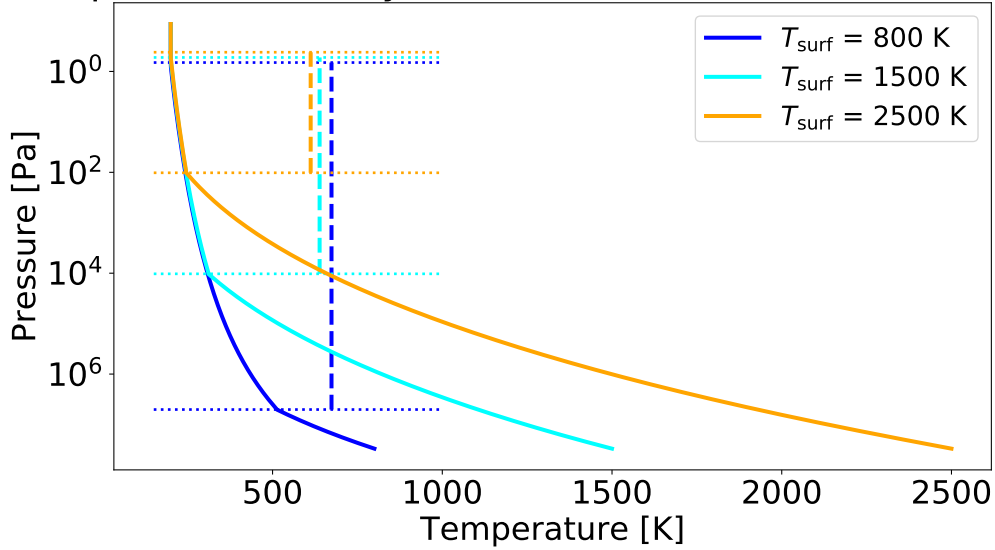
The atmospheric profile used in this model is separated in three (at most) physical layers ([Marcq *et al.*, 2017](#)), displayed in [Fig. 1](#) and [Fig. 2](#). From the bottom up: (1) an unsaturated troposphere, where heat transport is dominated by convective processes. The humidity ratio $\text{H}_2\text{O}/\text{CO}_2$ is constant in this layer. Then (2) a moist troposphere, saturated in water vapor, which is also a convective layer. It is in this layer that clouds are prescribed, considered as terrestrial clouds from a microphysical point of view (see [§2.1.4](#)). The dashed vertical lines in [Fig. 1](#) represent the vertical extent of this cloud layer for three different surface temperatures. The humidity ratio decreases with increasing height in the moist troposphere as shown in [Fig. 2](#). Please take note that if the moist troposphere reaches the ground, which happens whenever the partial surface pressure of H_2O at the surface exceeds the saturation pressure and if we are below the critical point of water, then an ocean of liquid water is expected to be formed on the surface of the planet ([Marcq *et al.*, 2017](#)) with the excess water content. Finally (3), a purely radiative, isothermal mesosphere with a temperature fixed to $T_0 = 200\text{ K}$ following other studies ([Lupu *et al.*, 2014](#); [Leconte *et al.*, 2013](#)) which have shown that even for very hot surface temperatures, these atmospheres exhibit rather cool temperatures at their top. In this layer, humidity remains constant (at a lower value: we have a cold trap) in the mesosphere. The analytical expressions for $\text{H}_2\text{O}/\text{CO}_2$ profiles are the same as in ([Kasting, 1988](#)). We focused our study on magma ocean planets located far enough to be able to cool, that is far enough of their host stars so that they absorb less than $\sim 300\text{ W/m}^2$ (Nakajima’s limit). In such a regime, most comparable studies find cool mesospheres ([Lupu *et al.*, 2014](#); [Leconte *et al.*, 2013](#)).

The radiative transfer is performed using the radiative standard solver DISORT ([Stamnes *et al.*, 1988](#)) in a four-stream approximation in order to compute the thermal emission in 36 spectral intervals (given in [Tab. 1](#)). For this, we use the correlated- k approach ([Fu & Liou, 1992](#)). We use 16 Gauss points in the g -space integration, where g is the cumulated distribution function of the spectrally-resolved line and continuum absorption data in each of the 36 bands. In order to calculate the opacity of the planetary atmosphere in the thermal range, the model makes use of the line opacities and continuum opacities of mixtures of CO_2 and H_2O , where both gases can become dominant.

2.1 Model update

The aim of this study is to determinate the Bond (or bolometric) albedo of MO planets. For this, we extended the spectral range of our model to optical and near UV domains. This implies some model improvements and

Atmospheric inventory: $P(\text{H}_2\text{O}) = 200 \text{ bar}$; $P(\text{CO}_2) = 100 \text{ bar}$



Atmospheric inventory: $P(\text{H}_2\text{O}) = 10 \text{ bar}$; $P(\text{CO}_2) = 500 \text{ bar}$

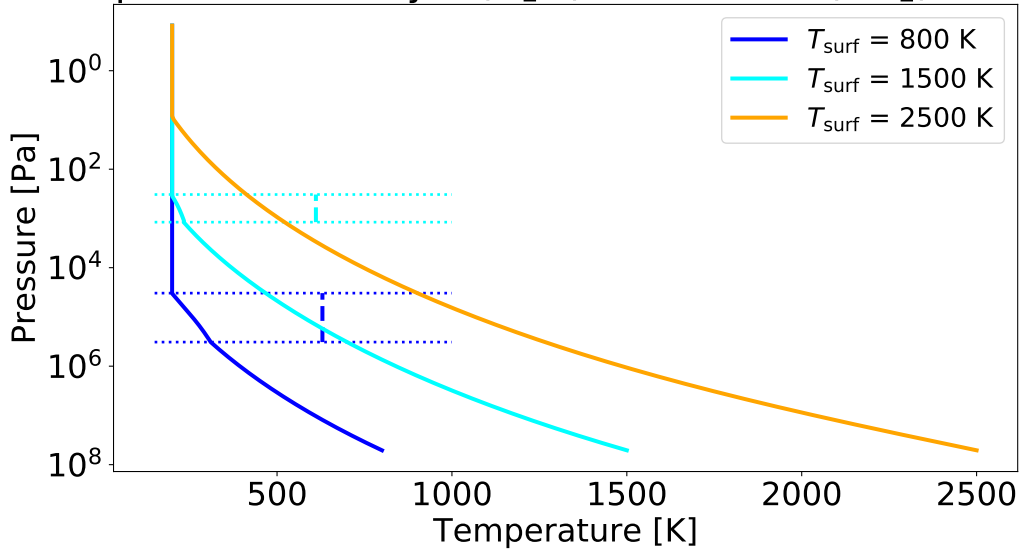


Figure 1: Temperature profiles for a water-dominated atmosphere (up) and a CO_2 -dominated atmosphere (down) at three surface temperatures using the model from [Marcq *et al.* \(2017\)](#). The horizontal dotted lines show the moist/dry troposphere limits and the moist troposphere/mesosphere limits for the three surface temperatures assumed. Finally, the vertical dotted lines delimit the cloud layer vertical extent for each surface temperature.

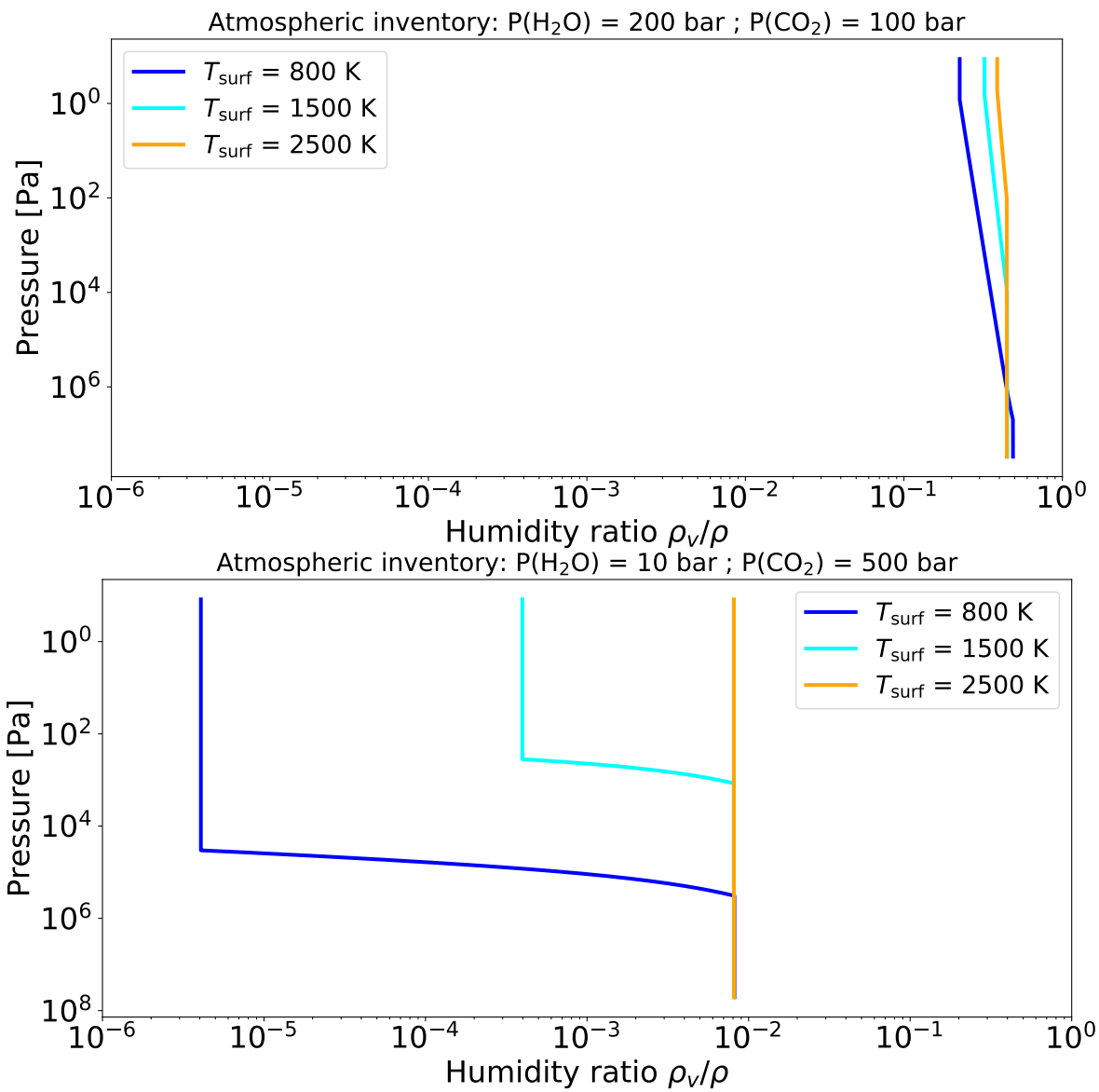


Figure 2: Humidity profile for a water-dominated atmosphere (up) and a CO₂-dominated atmosphere (down) at three surface temperatures using the model from [Marcq et al. \(2017\)](#).

Molecules	σ_0 [cm ² /molecule]	λ_0 [μ m]	Bibliographical references
H ₂ O	$2.5 \cdot 10^{-27}$	0.6	Kopparapu <i>et al.</i> (2013)
CO ₂	$1.24 \cdot 10^{-26}$	0.532	Sneep & Ubachs (2005)

Table 2: Table showing the Rayleigh scattering cross-sections and corresponding wavelengths for the two molecules used in our study.

modifications which are detailed in the following subsections.

2.1.1 Rayleigh scattering

Due to new shorter wavelength range under study, Rayleigh scattering opacity was added to the most recent version of the atmospheric submodule ([Marcq *et al.*, 2017](#)). Rayleigh cross-sections of H₂O and CO₂ were assumed to follow a simple λ^{-4} spectral dependency: $\sigma_{\text{Rayleigh}}(\lambda) = \sigma_0(\frac{\lambda_0}{\lambda})^4$ with σ_0 and λ_0 (given in Tab. 2) so that spectral averaging within each of the 36 bands in both thermal (1–200 μ m) and stellar (0.2857–5.1282 μ m) components could be computed analytically. Although the spectral dependency of $\sigma_{\text{rayleigh}}(\lambda)$ with the wavelength is actually more complex ([Sneep & Ubachs, 2005](#)), we used this simple analytical equation across the whole spectrum. This choice is justified because cross-sections have been estimated around a wavelength of 0.6 μ m, which is where the details of Rayleigh scattering opacity are most relevant (see also §3.1).

2.1.2 Gaseous line absorption

We used here new line opacity data supplementing those of [Marcq *et al.* \(2017\)](#). Opacity caused by the absorption of H₂O and CO₂ in the atmosphere has been computed using *kspectrum* ([Eymet *et al.*, 2016](#)) to yield high-resolution line-by-line spectra. We used the HITRAN2012 database for the H₂O and CO₂ line intensities and parameters ([Rothman *et al.*, 2013](#)). Additionally, we incorporated here the half-width at half maximum of H₂O lines broadened by CO₂ ($\gamma^{\text{H}_2\text{O}-\text{CO}_2}$) and CO₂ lines broadened by H₂O ($\gamma^{\text{CO}_2-\text{H}_2\text{O}}$), as well as the corresponding temperature dependence exponents ($n^{\text{H}_2\text{O}-\text{CO}_2}$ and $n^{\text{CO}_2-\text{H}_2\text{O}}$), based on references ([Brown *et al.*, 2007](#); [Sung *et al.*, 2009](#); [Gamache *et al.*, 2016](#); [Delahaye *et al.*, 2016](#)). More details can be found in [Turbet *et al.* \(2017b\)](#) and [Tran *et al.* \(2018\)](#). High resolution spectra were then computed using *kspectrum* ([Eymet *et al.*, 2016](#)), for a given temperature/pressure/composition grid, detailed in Tab. 3.

Given the range of temperatures/pressures probed here, and given the importance of continuum absorption in the dense atmosphere discussed here, we believe that – as of 2018 – the HITRAN database is more reliable for the calculations of absorption coefficients used in the present work than any other existing database, including ExoMol. Indeed, ExoMol cross-sections were calculated assuming H₂ and He-dominated atmospheres, i.e. assuming line broadening by H₂/He, whereas, in the present study, we used self-broadening coefficients $\gamma^{\text{CO}_2-\text{CO}_2}/\gamma^{\text{H}_2\text{O}-\text{H}_2\text{O}}$ provided by HITRAN and foreign broadening coefficients $\gamma^{\text{CO}_2-\text{H}_2\text{O}}/\gamma^{\text{H}_2\text{O}-\text{CO}_2}$ (and associated temperature dependency exponents $n^{\text{H}_2\text{O}-\text{CO}_2}/n^{\text{CO}_2-\text{H}_2\text{O}}$) described above. Plus, some band lines are missing from the ExoMol database. For instance, CO₂ band lines around 1300-1400 cm⁻¹ are missing from ExoMol. More generally, we recall that the widely used HITRAN database is based on both experiments and calculations, whereas ExoMol cross-sections/line lists are based on theoretical calculations only.

2.1.3 Continuum absorption

As we study dense atmospheres, we have to take into account collision induced absorption, dimer absorptions and far line wing absorptions. These absorptions are especially relevant to assess the transparency of possible spectral windows wherever line opacity is weak.

Far line wings of CO₂ (CO₂-CO₂ and CO₂-H₂O) were computed using the χ -factor approach as in [Tran *et al.* \(2018\)](#). This is an empirical correction of the Lorentzian line shape adjusted to laboratory measurements. CO₂-CO₂ collision-induced and dimer absorptions were computed based on references ([Gruszka & Borysow, 1997](#); [Baranov *et al.*, 2004](#); [Stefani *et al.*, 2013](#)).

H₂O-H₂O continuum was taken into account using the MT_CKD 3.0 database ([Mlawer *et al.*, 2012](#)), from 0 to 20,000 cm⁻¹. MT_CKD databases are available on <http://rtweb.aer.com/>. H₂O-CO₂ continuum was calculated with the line shape correction functions of [Ma & Tipping \(1992\)](#) using line positions and intensities from the HITRAN2012 database ([Rothman *et al.*, 2013](#)), with a cut-off distance at 25 cm⁻¹, and from 0 to 20,000 cm⁻¹. The temperature dependence of the continuum was empirically derived using data digitized from [Pollack *et al.* \(1993\)](#). More details can be found in [Turbet *et al.* \(2017b\)](#) and [Tran *et al.* \(2018\)](#).

Temperature/pressure/composition grid used in this study		
Pressure (Pa)	Temperature (K)	Volume mixing ratio (H ₂ O/(CO ₂ +H ₂ O))
10 ⁷	900	10 ⁻⁷
10 ⁶	700	10 ⁻⁶
10 ⁵	500	10 ⁻⁵
10 ⁴	420	10 ⁻⁴
10 ³	360	10 ⁻³
10 ²	300	10 ⁻²
10 ¹	250	10 ⁻¹
10 ⁰	200	3 × 10 ⁻¹
10 ⁻¹		7 × 10 ⁻¹
		9 × 10 ⁻¹
		9.9 × 10 ⁻¹

Table 3: Table showing the temperature/pressure/composition grid used to calculate gaseous absorption.

Wavelength λ [μm]	$\lambda < 2$	$2 \leq \lambda < 10$	$10 \leq \lambda < 20$	$20 \leq \lambda$
Single-scattering albedo ϖ_0	1	$1.24\lambda^{-0.32}$	$1.24\lambda^{-0.32}$	$1.24\lambda^{-0.32}$
Extinction efficiency Q_{ext}	1	1	1	$3.26\lambda^{-0.4}$
Asymmetry factor g	0.85	0.85	$1.4 \times \lambda^{-0.22}$	$1.4 \times \lambda^{-0.22}$

Table 4: Optical properties of clouds.

2.1.4 Cloud optical properties

In this updated model, we take into account the cloud opacity as in [Marcq *et al.* \(2017\)](#). We take into account the wavelength dependency of cloud opacity (see Tab. 4) according to approximated Mie theory calculations from [Kasting \(1988\)](#) and assuming spherical H₂O droplets with a mean 5 μm radius.

Following [Kasting \(1988\)](#), the mass loading of these Earth-like clouds is $\rho_{\text{clouds}} = 4 \cdot 10^{-4} \rho_{\text{gases}}$. Single scattering phase function is assumed to follow the analytical Henyey-Greenstein expression with the asymmetry parameter g given by [Kasting \(1988\)](#).

3 Results

3.1 Spectral reflectance & albedo

Now that we have taken Rayleigh scattering and atmospheric gaseous opacities into account as well as the Mie scattering from clouds, we can calculate the spectral reflectance of these atmospheres, as shown in Fig. 3. For this, we use the solver DISORT ([Stamnes *et al.*, 1988](#)) and assume a mean isotropic illumination at the top of the atmosphere. We can see on Fig. 3 that the spectral reflectance with or without clouds is very high under 0.5 μm due to very efficient Rayleigh scattering at shorter wavelengths.

Beyond 0.5 μm , the behavior of the spectral reflectance strongly depends on the surface temperature of the planet and whether clouds are taken into account or not. Without clouds in the atmosphere, there is a competition between Rayleigh scattering and gaseous absorption. Overall, Rayleigh scattering fails to compensate for H₂O and CO₂ absorption in the near infrared resulting in a rapid collapse of spectral reflectance at smaller wavenumbers, as shown by the dashed lines in Fig. 3. Nevertheless, there are still local reflectance maxima where gaseous absorption is very low (spectral windows).

When clouds are taken into account, we no longer observe a collapse of the spectral reflectance towards smaller wavenumbers, but a more modest decrease by one order of magnitude. This is due to the contribution of Mie scattering to spectral reflectance. However, we then observe two distinct behaviors of the spectral reflectance at smaller wavenumbers. Firstly, it depends primarily on the surface temperature: the higher the surface temperature for a given atmosphere, the thinner the cloud layer and its reflectance is reduced. Secondly, for any given surface temperature, the spectral reflectance is decreasing with decreasing short wavenumber. Indeed, Mie scattering becomes less and less efficient at smaller wavenumber (see Tab. 4). Also, we can note some spectral structure in the spectral reflectance, which is due to absorption bands of H₂O and CO₂ in the near infrared even in the presence

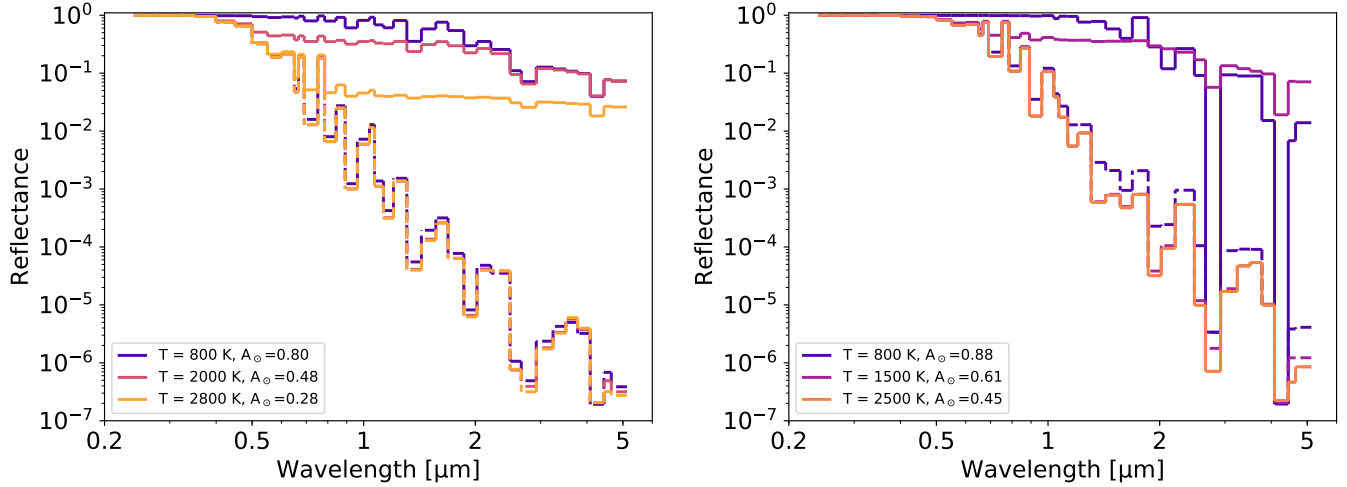


Figure 3: Spectral reflectance with clouds (solid curve) and without clouds (dashed curve), for three different surface temperatures. For spectral reflectance with clouds, the corresponding Bond albedo for a Sun-like star is indicated. The sharp variations in reflectance are due to molecular absorption bands, such as at the 2.7 μm (H_2O) and the 4.3 μm (CO_2) features. Atmospheric inventory : (left) $P_{\text{H}_2\text{O}} = 200$ bar, $P_{\text{CO}_2} = 100$ bar. (right) $P_{\text{H}_2\text{O}} = 10$ bar, $P_{\text{CO}_2} = 500$ bar.

of clouds – typically water absorption bands at about 2.7 μm and carbon dioxide absorption at about 4.3 μm (see Fig. 3).

Once the spectral reflectance is computed, the resulting Bond albedo can be calculated by weighting the reflectivity of each band of the 36 bands according to the stellar emission, assuming that it behaves like a blackbody of effective temperature T_* at the studied wavelengths. This yields the following formula:

$$A_B(R; T_*) = \frac{\int_0^\infty R(\tilde{\nu}) B_{\tilde{\nu}}(T_*) d\tilde{\nu}}{\int_0^\infty B_{\tilde{\nu}}(T_*) d\tilde{\nu}} = \frac{\pi \int_0^\infty R(\tilde{\nu}) B_{\tilde{\nu}}(T_*) d\tilde{\nu}}{\sigma T_*^4}$$

where $R(\tilde{\nu})$ stands for the spectral reflectance as a function of wavenumber, $B_{\tilde{\nu}}(T_*)$ the Planck as a function of wavenumber and stellar temperature and σ the Stefan-Boltzmann constant.

3.2 Albedo behavior with respect to surface temperature

The typical behavior of the Bond albedo with respect to the surface temperature is shown in Fig. 4 for a MO planet with an atmospheric composition dominated by water vapor, and taking clouds into account. Our model is unidimensional, therefore the clouds cover the entire planet. This seems reasonable to assume that such MO planets are either totally covered by clouds, as Venus today, or either totally cloudless, because these atmospheres are dominated by their internal heat flux. It has actually been demonstrated with a 3-Dimensions Global Climate Model that a complete cloud cover would be produced following very large meteoritic impact events (Turbet *et al.*, 2017a), while the thermal budget of the atmosphere is dominated by the infrared cooling of the atmosphere of the planet. More generally, the internal heat flux of MO planets should not strongly depend on local time or latitude, so that we expect much more horizontally uniform atmospheres than for atmospheres dominated by the stellar flux. This Fig. 4 reveals three main features:

1. For relatively low surface temperatures, the planet exhibits a very high and temperature-independent albedo (about 0.8 – 0.9 here). This is due to the Mie scattering in the clouds completely dominating the gaseous absorption. Backscattered photons travel a short optical path in the atmosphere and are then less absorbed. This situation is comparable to Venus, which also exhibits a very high albedo due to its thick uniform cloud cover.
2. For intermediate surface temperatures, the albedo decreases gradually with increasing surface temperature. Indeed, when the surface temperature increases, the cloud layer vertical extent and more importantly, the cloud layer optical depth (in the moist troposphere) shrinks (see Fig. 1 and Fig. 2). The cloud base moves upwards, at pressure levels where the mass loading of these clouds is much lower. The Mie scattering becomes less efficient compared to the gaseous absorption, mostly unaffected by changes in cloud content.

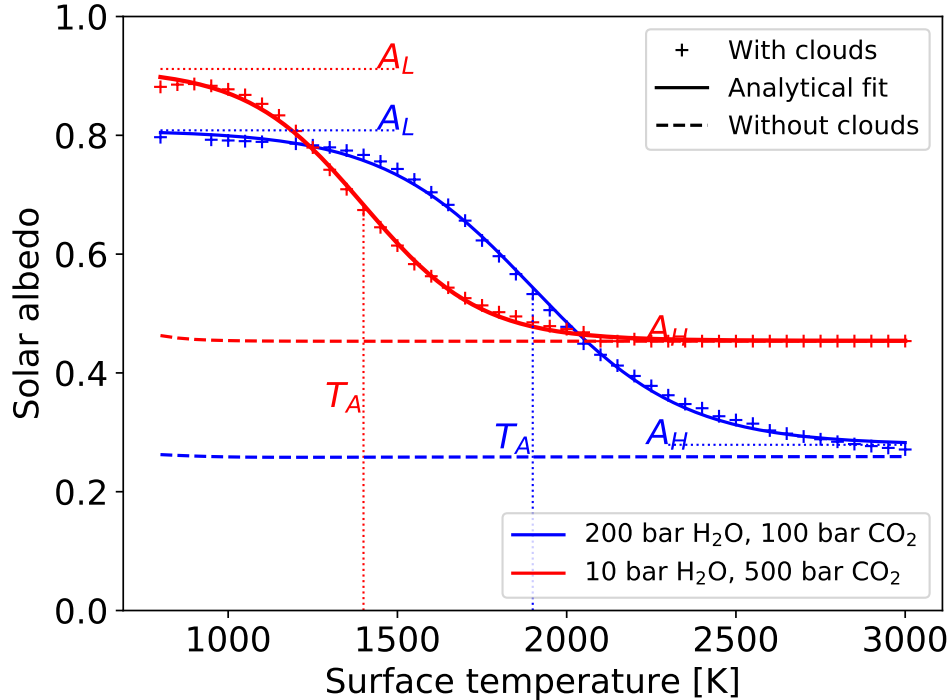


Figure 4: Bond albedo as a function of surface temperature as computed by our model (crosses) and our analytic fit (solid) for two different atmospheres, H₂O-dominated (blue) and CO₂-dominated (red) illuminated by the Sun ($T_* = 5750$ K). The above plot indicates that, the planet has a high albedo at low surface temperatures due to Mie scattering dominating the gas absorption. At high surface temperatures, the albedo reaches asymptotic value of 0.25, consistent with Hamano *et al.* (2015), due to dominance of the gas absorption. Intermediate temperatures result in decreasing albedo due to the shrinkage of the cloud deck, as shown in Fig. 1.

3. For very high surface temperatures, the albedo decreases towards an asymptotic value (at 0.25 here), which corresponds to the albedo of a cloudless atmosphere. In this domain, relatively inefficient Rayleigh scattering is the only counterpart to gaseous absorption since Mie scattering by the clouds has become negligible. The value of 0.25 is rather in good agreement with the work of Hamano *et al.* (2015) who found an albedo of 0.22 for such high temperatures and similar atmospheric composition.

The qualitative trends described above are independent of the atmospheric composition for all the 42 compositions that we modeled (see Tab. 5). An illustration of this is shown in Fig. 4 for two different atmospheres, H₂O-dominated (blue) and CO₂-dominated (red).

In order to investigate the effects of varying e.g. the atmospheric composition, we sought to extract some meaningful parameters from the curves $A_B = f(T_{\text{surf}})$. The empirical analytical fit:

$$A_B(T_{\text{surf}}) = \left(\frac{A_L - A_H}{2} \right) \tanh \left(\frac{T_A - T_{\text{surf}}}{T_{\text{scale}}} \right) + \frac{A_H + A_L}{2}$$

yields a surprisingly good fit (Fig. 4) of our modeling. Here, T_A defines our *albedo transition temperature* between the two regimes described above. In other words, T_A is the surface temperature yielding an intermediate albedo ($\frac{A_L + A_H}{2}$), where A_H and A_L respectively stand for the high- and low-temperature asymptotic values of the albedo. Finally T_{scale} corresponds to the temperature range where the albedo transition occurs. T_{scale} is the extent of the surface temperature domain centered on T_A where the albedo lies in the 12-88 % interval between A_L and A_H . T_{scale} appears to be on the order of 400 ± 40 K for all investigated atmospheres, as shown in Fig. 5 .

3.3 Albedo vs. atmospheric inventory

As stated in the introduction, the atmospheres considered in this model of MO planets are only composed of H₂O and CO₂ (Lupu *et al.*, 2014). It is possible that these atmospheres were dominated by other species, and our

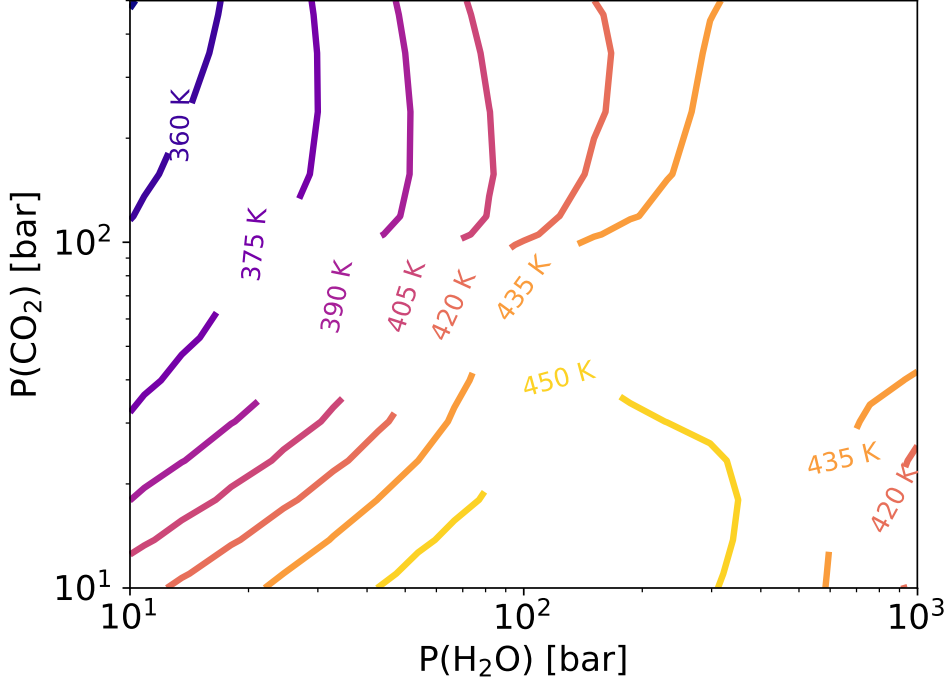


Figure 5: Contour plot of the temperature interval width T_{scale} where the albedo transition occurs with respect to the partial pressures $P_{\text{surf}}(\text{H}_2\text{O})$ and $P_{\text{surf}}(\text{CO}_2)$ for a planet around by the Sun ($T_* = 5750 \text{ K}$).

$P_{\text{surf}}(\text{H}_2\text{O})$ [bar]	10	20	50	100	200	500	1000
$P_{\text{surf}}(\text{CO}_2)$ [bar]	10	20	50	100	200	500	N/A
T_{surf} [K]	800–3000 ; step of 50						

Table 5: T_{surf} , H_2O and CO_2 pressure grid used to simulate $7 \times 6 = 42$ different atmospheric inventories and surface temperature grid (45 points).

results indeed do show that atmospheric inventory has an impact on their albedo. To analyse this impact, we ran our model for 42 compositions according to the composition grid in Tab. 5.

We then investigated how our previously derived quantities (T_A , A_H , A_L) changed with the atmospheric inventory. Fig. 7 shows transition temperature albedo's behavior T_A according to the H_2O and the CO_2 partial pressures. This figure shows that this transition temperature occurs at higher values when atmospheric water content increases. Indeed, for a given surface temperature, the more water available the optically thicker the cloud layer (as shown in Fig. 1 and Fig. 2), so that the albedo remains high over a wider range of surface temperatures, up to 2400 K for our largest investigated water content value (1000 bar). On the other hand, CO_2 has a marginal opposite effect, lowering the humidity and therefore cloud opacity, all other parameters kept the same. This behavior is reminiscent of the behavior of the threshold temperature T_ε defined by Marcq *et al.* (2017) as the surface temperature T_s where the effective emissivity $\varepsilon(T_s) = \text{OLR}(T_s)/\sigma T_s^4$ reaches its minimal value. This threshold temperature determines the transition between the low temperature regime $T_s < T_\varepsilon$ where OLR is relatively low and constant ("runaway" regime) and the high temperature regime $T_s > T_\varepsilon$ where OLR increases significantly with increasing T_s ("post-runaway" regime).

We therefore plotted T_ε vs. T_A on Fig. 6. This figure shows that these two temperature are actually the same within a constant offset ($T_\varepsilon - T_A \simeq 240 \text{ K}$), which testifies to the fact that the vertical structure of the atmosphere determines both its thermal emission and its albedo. As the surface temperature increases, clouds are becoming thinner, the albedo decreases and the upper layers become hot enough for the thermal radiation to substantially increase. Conversely, relatively cool MO planets harbor both optically thick clouds (yielding a high albedo) and a small outgoing thermal flux, close to 280 W/m^2 when water vapor dominates the NIR spectrum, see Marcq *et al.* (2017).

For surface temperatures smaller than the albedo transition temperature T_A , the asymptotic low temperature

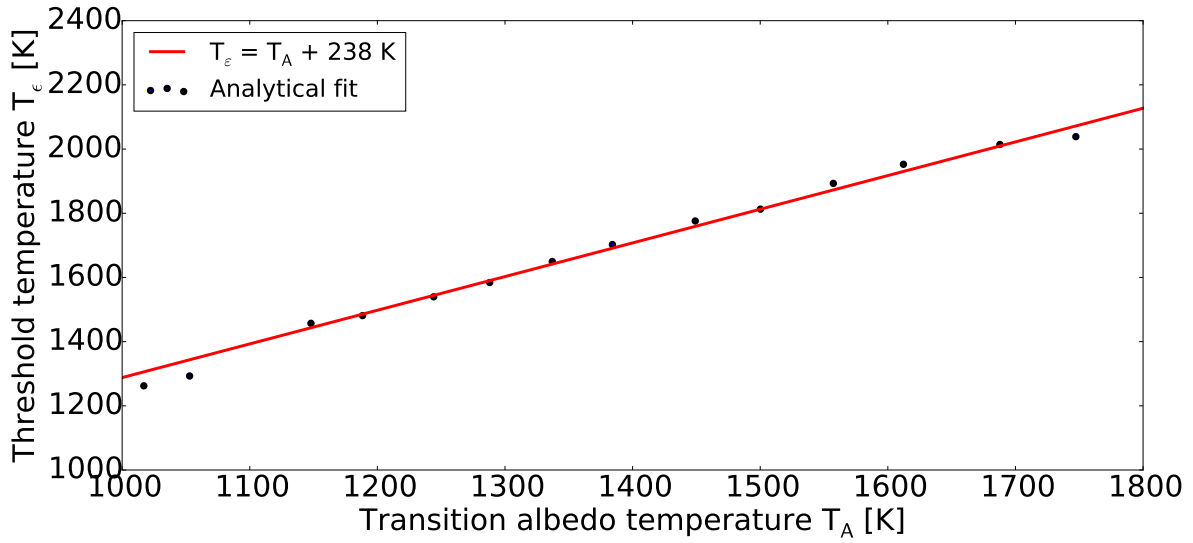


Figure 6: Threshold temperature T_ϵ with respect to the albedo transition temperature T_A (black dots) and its linear fit (solid red).

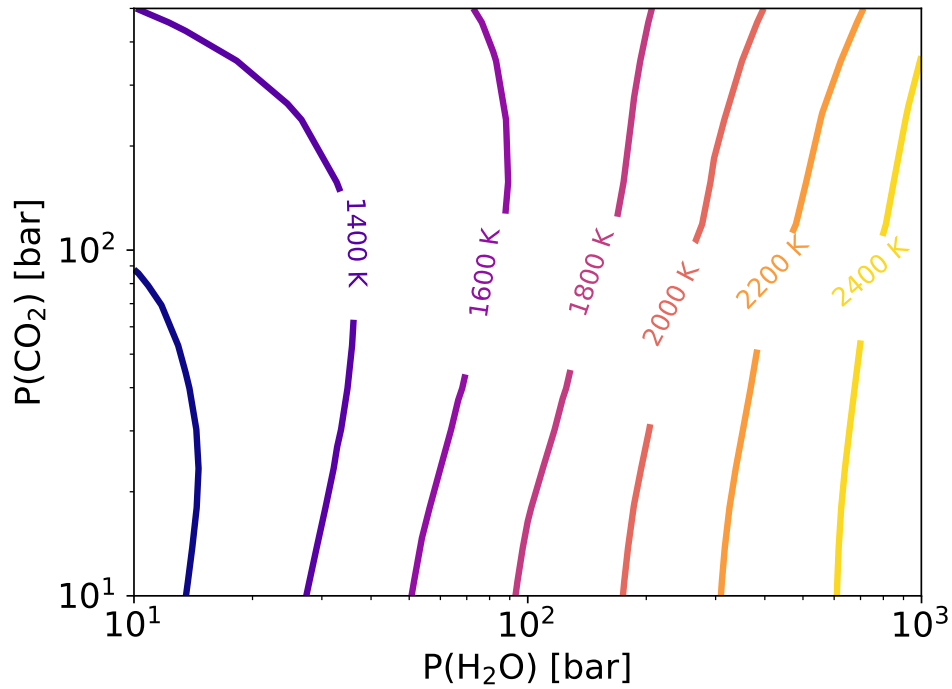


Figure 7: Contour plot of the albedo transition temperature T_A with respect to the partial pressures $P_{\text{surf}}(\text{H}_2\text{O})$ and $P_{\text{surf}}(\text{CO}_2)$ for a planet around by the Sun ($T_* = 5750 \text{ K}$).

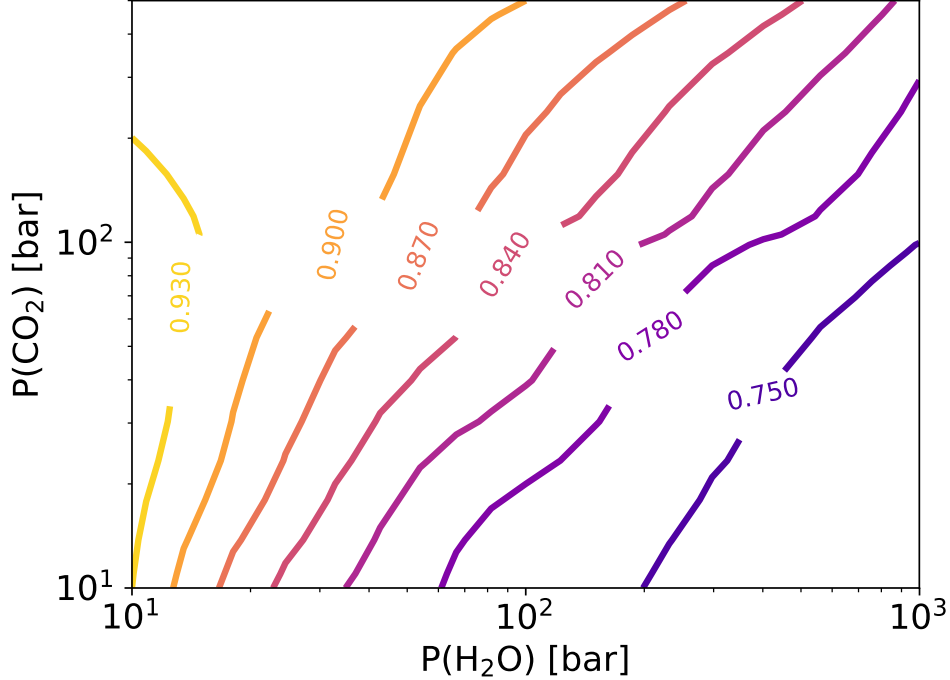


Figure 8: A_L contour plot with respect to H_2O partial pressure $P_{\text{surf}}(\text{H}_2\text{O})$ and CO_2 partial pressure $P_{\text{surf}}(\text{CO}_2)$, taking into account the effects of cloud and assuming a Sun-like star ($T_* = 5750 \text{ K}$).

albedo A_L exhibits a fairly simple behavior. On one hand, Fig. 8 shows that for a given CO_2 partial pressure, the albedo increases when the pressure in H_2O decreases. On the other hand, for a given H_2O partial pressure, the albedo increases when the partial pressure in CO_2 increases. These two statements reflect the same physical phenomenon, namely that H_2O is a stronger absorber of stellar radiation than CO_2 , especially in the near IR. Drier atmospheres above the cloud top absorb less, therefore increasing the albedo (since the single scattering albedo of cloud particles is assumed to be close to unity for $\lambda < 2 \mu\text{m}$). The very high values for A_L for dry atmospheres are however not very robust, since any trace contaminant in the clouds would significantly lower the albedo (as it is indeed the case with Venus, whose Bond albedo of 0.7 is lower than we would assume from Fig. 8).

For surface temperatures higher than the albedo transition temperature, the albedo shows two distinct trends as we can see on Fig. 9. Please remember that for $T_{\text{surf}} \gg T_A$, cloud scattering becomes negligible and that only Rayleigh scattering contributes to the albedo. For very hot surface temperature, the cloud layer is indeed very thin when the atmosphere is water-dominated (Fig. 1 left and Fig. 2 left) or even nonexistent for atmosphere CO_2 -dominated (Fig. 1 right and Fig. 2 right). When H_2O partial pressure is relatively low, the albedo A_H exhibits the same behavior than A_L in Fig. 8. This behavior is consistent with the work of [Kopparapu *et al.* \(2013\)](#) who showed that the albedo increases from 0.3 to 0.5 with partial pressure of CO_2 increasing from 1 to 35 bar. These values are comparable to the albedos on Fig. 9 which range from 0.28 to 0.40. On the other hand, when H_2O surface pressure is higher than about 10 times than CO_2 surface pressure, the albedo is increasing with $P_{\text{surf}}(\text{H}_2\text{O})$ instead, with little dependency with respect to $P_{\text{surf}}(\text{CO}_2)$. This is because, for such high partial pressures of H_2O , line opacity is quickly saturated, and most of the reflectivity occurs in spectral windows of H_2O , so that water opacity is mostly due to the H_2O - H_2O continuum. Also, the effective Rayleigh scattering level (for $\tau_{\text{ray}} \sim 1$) occurs at a more or less constant pressure (close to a few bars), but the temperature at these pressures is increasing with $\text{H}_2\text{O}/\text{CO}_2$ ratio due to the larger lapse rate of H_2O compared to CO_2 (keeping in mind that the temperature at vanishing pressures is always close to 200 K, see Fig. 1). It appears that H_2O - H_2O continuum opacity is greatly reduced at temperatures higher than about 500 K, reached at these pressures level in this $\text{H}_2\text{O}/\text{CO}_2$ domain, therefore yielding a counter-intuitive increase in albedo with increasing $P_{\text{surf}}(\text{H}_2\text{O})$. This results are however considered not very robust, since the details of H_2O - H_2O continuum opacity are poorly known at such high temperatures (our tabulated values from MT_CKD 3.0 are capped at a temperature of 700 K).

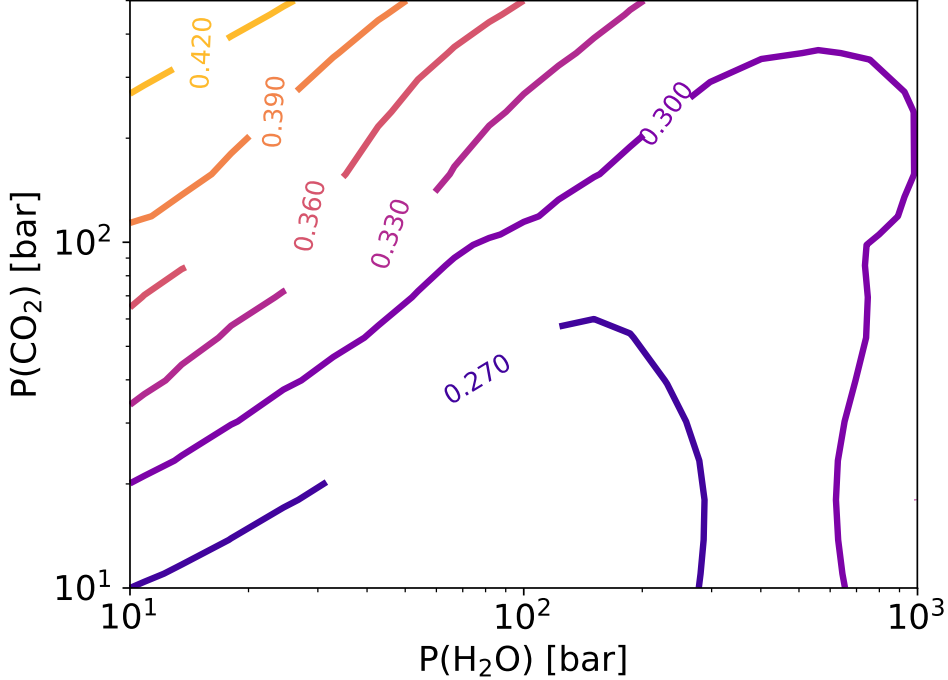


Figure 9: A_H contour plot with respect to $P_{\text{surf}}(\text{H}_2\text{O})$ and $P_{\text{surf}}(\text{CO}_2)$, assuming a Sun-like star ($T_* = 5750$ K).

3.4 Albedo vs. star temperature

Since our modeled reflectivity is not constant in the visible-near IR range, stellar temperature T_* obviously impacts planetary albedo. We show in Fig. 10 the Bond albedo of MO planets as a function of the star temperature for the standard atmosphere inventory ($P_{\text{surf}}(\text{H}_2\text{O}) = 200$ bar; $P_{\text{surf}}(\text{CO}_2) = 100$ bar), with and without clouds, and for a surface temperature $T_{\text{surf}} = 800$ K. As expected, the albedo is increasing with increasing stellar temperatures in both cases.

The reasons for this behavior are twofold. Firstly, the clouds absorb more and more at wavelengths longer than $2\ \mu\text{m}$ (see Tab. 4). Secondly, Rayleigh scattering becomes negligible for wavelengths longer than about $1\ \mu\text{m}$. Our results are moreover in agreement with [Kopparapu *et al.* \(2013\)](#), who previously showed that the Bond albedo increases with stellar temperature. We get Bond albedos of 0.03 and 0.07 for an atmosphere illuminated by 3000 K and 3800 K M-dwarfs respectively, and [Kopparapu *et al.* \(2013\)](#) find 0.01 and 0.04 for similar planets illuminated by 2600 K and 3800 K M-dwarfs, respectively. The small differences between their study and ours are probably due to differences in composition (their atmospheres contain almost no CO_2 unlike ours) and H_2O - H_2O continua values (MT_CKD 3.0 in our study, BPS in [Kopparapu *et al.* \(2013\)](#)).

According to Fig. 10, the increase of albedo in the cloudless case is comparatively stronger than the increase of the cloudy albedo. The latter also exhibits some saturation once the stellar effective temperature reaches about 6000 K. Indeed, our 1D model forces an altitude to the cloud layer according to the surface temperature of the planet. The Fig. 10 shows a relatively cold planet ($T_{\text{surf}} = 800\ \text{K} \ll T_A$) which exhibits a thick and dense cloud layer located at low altitude. One should note that spectral reflectance of the clouds is considered equal to 1 for wavelengths smaller than $2\ \mu\text{m}$ (Tab. 4). Hotter stars with emission peaks shifted to shorter wavelengths therefore results in an increased albedo. Once the star is hot enough, most of its emission falls below $2\ \mu\text{m}$. This explains the saturation of the albedo for hotter stars observed on Fig. 10 when clouds are taken into account. On the other hand, the albedo for cloudless atmosphere increases almost linearly with respect to the star temperature. Indeed, without clouds, only Rayleigh scattering contributes to the albedo increases, and Rayleigh scattering is more and more efficient at shorter wavelengths. Therefore, the impact of the star's temperature is significantly more dramatic for cloudless atmospheres.

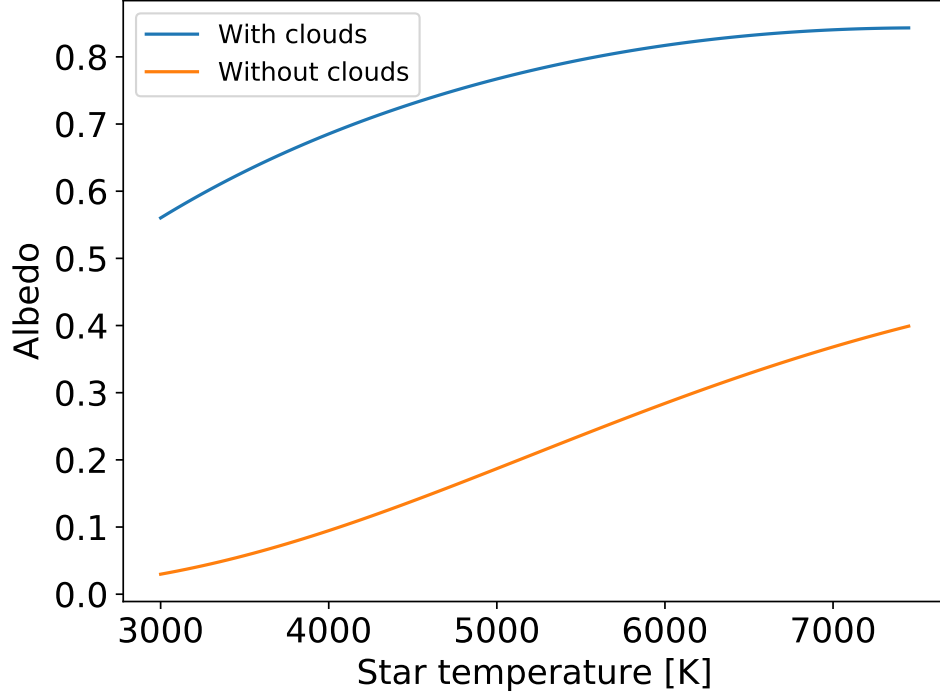


Figure 10: Albedo at low surface temperature (A_L) with clouds (blue) and without clouds (orange) taken into account for a water-dominated atmosphere as a function of star temperature. Atmospheric inventory : $P_{\text{surf}}(\text{H}_2\text{O}) = 200$ bar; $P_{\text{surf}}(\text{CO}_2) = 100$ bar.

4 Limitations

4.1 Temperature profile

In the current version of our model, the mesospheric temperature is fixed at 200 K (Marcq, 2012; Marcq *et al.*, 2017). Our model does not take into account the heating induced by the visible and UV radiation from the star, and therefore does not allow for the emergence of a possible stratosphere (defined as an atmospheric layer where $dT/dz > 0$). The temperature profile could affect the Bond albedo of the planet in an indirect way, through changes in the cloud opacity.

Note that the Bond albedo for cloudy atmosphere MO planets is significantly higher than in Kopparapu *et al.* (2013) (Figure 3b), because clouds are not taken into account in their work. It is tempting to believe that the Bond albedo calculated in our study could change the fate of planets going into runaway greenhouse, as such planets should behave in the same way as cool MO planets described in our work. As a planet warms up and goes into runaway greenhouse, a thick reflective cloud cover forms and stabilizes the climate of the planet. However, our calculations neglected 1) the effect of the incoming stellar radiation on the temperature profile and thus on cloud formation and 2) 3-D atmospheric circulation processes that can control the formation and properties of clouds (Leconte *et al.*, 2013). Formation of clouds and their impact on the fate of planets going into runaway greenhouse could be tested in the future with 3-D Global Climate Model simulations taking into account clouds.

4.2 Opacity data

Although we regularly consider pressures over both critical pressures of H_2O and CO_2 , we usually do so at temperatures much larger than their respective critical temperatures, so that the departure with ideal gas is limited, especially for CO_2 . Also, for dense atmospheres most of backscattering occurs at relatively low pressures fully within our look-up tables, even more so when considering cloud opacity. It is nevertheless true that for relatively thin and hot atmospheres (therefore cloudless), we have non negligible contribution of layers hotter than 1000 K to the backscattering. In such a case our results are actually dependent of the poorly known opacities at these temperatures/pressures.

4.3 Cloud parameterization

Another limitation is the parameterization of clouds. We have indeed considered current terrestrial type clouds following [Kasting \(1988\)](#). But these clouds are probably inappropriate for some temperature profiles, especially when the clouds are very high in the atmosphere. Plus, temperature near the top of the cloud layer is below 273 K, so that we expect water ice clouds rather than liquid clouds. However, preliminary testing with 10-micron ice particles instead of 10-micron liquid water droplets only yield minor changes in resulting albedo (less than 2%), with a slightly higher albedo around G-stars and slightly lower around M-stars, consistent with the lower single scattering albedo of water ice compared to liquid water in the near infrared. We should also note that altering cloud microphysics (vertical mass loading profile, size distribution, contaminants, etc.) could have a more significant impact on our results. This highlights the need for a self-consistent microphysical scheme in future versions of our model.

4.4 Mesospheric temperature

An important point concerns the mesospheric temperature. As stated in Section 2, the mesospheric temperature is fixed in our model at 200 K. In fact, depending on the temperature of the host star and the irradiation received by the planet, the mesosphere could be more or less heated. We tested our results for three different mesospheric temperatures (150 K, 200 K and 250 K) and found that the bond albedo is the same for the cooler mesospheric temperature (150 K). For a mesospheric temperature of 250 K, the albedo decreases by less than 2-3% , due to an increase in mesospheric humidity.

4.5 Realistic star spectra

To calculate the MO planetary albedo, we made the approximation that the stars emitted like blackbodies.

However, while this assumption is quite correct for G-stars, it is much less so for colder stars (M-dwarfs) because the atmospheres of these stars are more complex. For example, Proxima Centauri’s spectrum, which is now well constrained by observations, displays an absorber in its atmosphere, especially in the visible around 0.4 and 0.6 μm and in the near UV around 0.3 μm ([Ribas *et al.*, 2017](#)). Therefore, the incident spectrum flux at the top of the atmosphere of the MO planet contains less visible and UV flux compared to a black body spectrum which should further lower the albedo of the planet in this case.

5 Conclusion

This paper presents a simple investigation of the albedo of MO planets. Our updated model allowed us to calculate the albedo of MO planets for surface temperatures between 800 and 3000 K for a large array of H_2O - CO_2 atmospheric inventories and for various star spectral type. This study has evidenced the strong influence of clouds (whenever present) on the Bond albedo. The albedo can become very high (larger than 0.9) when the clouds are optically thick. We have also shown that the composition of the atmosphere, and in particular the mixing ratio $\text{CO}_2/\text{H}_2\text{O}$, plays a key role on the albedo. Our work is in agreement with those of [Kopparapu *et al.* \(2013\)](#) and [Hamano *et al.* \(2015\)](#). Besides, we have shown that the spectral type of the host star strongly influences the resulting albedo in the same way that [Kopparapu *et al.* \(2013\)](#) did. Our results finally show that the variations of the albedo with respect to surface temperature can be parameterized with a precision better than 5% using a small number of quantities (asymptotic values at high and low surface temperature, transition temperature).

The next step of this research project is to make all the improvements presented above and then incorporate them all into a Global Climate Model (GCM) to simulate the cooling phase of young telluric planets. We could thus be able to better simulate the transition phase when the internal heat flux of the planet becomes negligible in front of the received stellar flux and thus we could have a more precise idea of the potential habitability of these planets. A second major challenge would be to use the spectral data and the albedo provided by our atmospheric model to compare them with the instrumental data expected from the space missions that will very soon study exoplanets such as the James-Webb Space Telescope (JWST) which will be launched by NASA/ESA in 2020.

6 Acknowledgement

This project has received funding from the European Research Council (ERC) under the European Union’s Horizon 2020 research and innovation programme (grant agreement n° 679030/WHIPLASH). EM acknowledges the support

References

- Baranov, Y. I., Lafferty, W. J., & Fraser, G. T. 2004. Infrared spectrum of the continuum and dimer absorption in the vicinity of the O₂ vibrational fundamental in O₂/CO₂ mixtures. *Journal of Molecular Spectroscopy*, **228**(Dec.), 432–440.
- Brown, L. R., Humphrey, C. M., & Gamache, R. R. 2007. CO₂-broadened water in the pure rotation and ν_2 fundamental regions. *Journal of Molecular Spectroscopy*, **246**(Nov.), 1–21.
- Delahaye, T., Landsheere, X., Panguì, E., Huet, F., Hartmann, J.-M., & Tran, H. 2016. Broadening of CO₂ lines in the 4.3 μm region by H₂O. *Journal of Molecular Spectroscopy*, **326**(Aug.), 17–20.
- Eymet, V., Coustet, C., & Piaud, B. 2016 (Jan.). kspectrum: an open-source code for high-resolution molecular absorption spectra production. *Page 012005 of: Journal of Physics Conference Series*. Journal of Physics Conference Series, vol. 676.
- Fu, Qiang, & Liou, K. N. 1992. On the Correlatedk-Distribution Method for Radiative Transfer in Nonhomogeneous Atmospheres. *Journal of the Atmospheric Sciences*, **49**(22), 2139–2156.
- Gamache, R. R., Farese, M., & Renaud, C. L. 2016. A spectral line list for water isotopologues in the 1100–4100 cm⁻¹ region for application to CO₂-rich planetary atmospheres. *Journal of Molecular Spectroscopy*, **326**(Aug.), 144–150.
- Gruszka, M., & Borysow, A. 1997. Roto-Translational Collision-Induced Absorption of CO₂ for the Atmosphere of Venus at Frequencies from 0 to 250 cm⁻¹, at Temperatures from 200 to 800 K. *Icarus*, **129**(Sept.), 172–177.
- Hamano, K., Kawahara, H., Abe, Y., Onishi, M., & Hashimoto, G. L. 2015. Lifetime and Spectral Evolution of a Magma Ocean with a Steam Atmosphere: Its Detectability by Future Direct Imaging. *ApJ*, **806**(June), 216.
- Kasting, James F. 1988. Runaway and moist greenhouse atmospheres and the evolution of Earth and Venus. *Icarus*, **74**(3), 472–494.
- Kopparapu, R. K., Ramirez, R., Kasting, J. F., Eymet, V., Robinson, T. D., Mahadevan, S., Terrien, R. C., Domagal-Goldman, S., Meadows, V., & Deshpande, R. 2013. Habitable Zones around Main-sequence Stars: New Estimates. *ApJ*, **765**(Mar.), 131.
- Lebrun, T., Massol, H., Chassefière, E., Davaille, A., Marcq, E., Sarda, P., Leblanc, F., & Brandeis, G. 2013. Thermal evolution of an early magma ocean in interaction with the atmosphere. *Journal of Geophysical Research: Planets*, **118**(6), 1155–1176.
- Leconte, Jérémy, Forget, Francois, Charnay, Benjamin, Wordsworth, Robin, & Pottier, Alizée. 2013. Increased insolation threshold for runaway greenhouse processes on Earth-like planets. *Nature*, **504**(7479), 268–271.
- Lupu, R. E., Zahnle, K., Marley, M. S., Schaefer, L., Fegley, B., Morley, C., Cahoy, K., Freedman, R., & Fortney, J. J. 2014. The Atmospheres of Earthlike Planets after Giant Impact Events. *ApJ*, **784**(Mar.), 27.
- Ma, Q., & Tipping, R. H. 1992. A far wing line shape theory and its application to the foreign-broadened water continuum absorption. III. *J. Chem. Phys.*, **97**(July), 818–828.
- Marcq, E. 2012. A simple 1-D radiative-convective atmospheric model designed for integration into coupled models of magma ocean planets. *Journal of Geophysical Research: Planets*, **117**(E1), n/a–n/a.
- Marcq, E., Salvador, A., Massol, H., & Davaille, A. 2017. Thermal radiation of magma ocean planets using a 1-D radiative-convective model of H₂O-CO₂ atmospheres. *Journal of Geophysical Research (Planets)*, **122**(July), 1539–1553.
- Mlawer, E. J., Payne, V. H., Moncet, J.-L., Delamere, J. S., Alvarado, M. J., & Tobin, D. C. 2012. Development and recent evaluation of the MT_CKD model of continuum absorption. *Philosophical Transactions of the Royal Society of London Series A*, **370**(June), 2520–2556.

- Pollack, James B., Dalton, J. Brad, Grinspoon, David, Wattson, Richard B., Freedman, Richard, Crisp, David, Allen, David A., Bezaud, Bruno, DeBergh, Catherine, Giver, Lawrence P., Ma, Q., & Tipping, Richard. 1993. Near-Infrared Light from Venus' Nightside: A Spectroscopic Analysis. *Icarus*, **103**(1), 1 – 42.
- Ribas, I., Gregg, M. D., Boyajian, T. S., & Bolmont, E. 2017. The full spectral radiative properties of Proxima Centauri. *A&A*, **603**(July), A58.
- Rothman, L. S., Gordon, I. E., Babikov, Y., Barbe, A., Chris Benner, D., Bernath, P. F., Birk, M., Bizzocchi, L., Boudon, V., Brown, L. R., Campargue, A., Chance, K., Cohen, E. A., Coudert, L. H., Devi, V. M., Drouin, B. J., Fayt, A., Flaud, J.-M., Gamache, R. R., Harrison, J. J., Hartmann, J.-M., Hill, C., Hodges, J. T., Jacquemart, D., Jolly, A., Lamouroux, J., Le Roy, R. J., Li, G., Long, D. A., Lyulin, O. M., Mackie, C. J., Massie, S. T., Mikhailenko, S., Müller, H. S. P., Naumenko, O. V., Nikitin, A. V., Orphal, J., Perevalov, V., Perrin, A., Polovtseva, E. R., Richard, C., Smith, M. A. H., Starikova, E., Sung, K., Tashkun, S., Tennyson, J., Toon, G. C., Tyuterev, V. G., & Wagner, G. 2013. The HITRAN2012 molecular spectroscopic database. *J. Quant. Spec. Radiat. Transf.*, **130**(Nov.), 4–50.
- Salvador, A., Massol, H., Davaille, A., Marcq, E., Sarda, P., & Chassefière, E. 2017. The relative influence of H₂O and CO₂ on the primitive surface conditions and evolution of rocky planets. *JGR-Planets*.
- Sneep, Maarten, & Ubachs, Wim. 2005. Direct measurement of the Rayleigh scattering cross section in various gases. *Journal of Quantitative Spectroscopy and Radiative Transfer*, **92**(3), 293 – 310.
- Stamnes, Knut, Tsay, S-Chee, Wiscombe, Warren, & Jayaweera, Kolf. 1988. Numerically stable algorithm for discrete-ordinate-method radiative transfer in multiple scattering and emitting layered media. *Applied Optics*, **27**(12), 2502.
- Stefani, S., Piccioni, G., Snels, M., Grassi, D., & Adriani, A. 2013. Experimental CO₂ absorption coefficients at high pressure and high temperature. *J. Quant. Spec. Radiat. Transf.*, **117**(Mar.), 21–28.
- Sung, K., Brown, L. R., Toth, R. A., & Crawford, T. J. 2009. Fourier transform infrared spectroscopy measurements of H₂O-broadened half-widths of CO₂ at 4.3 μm . This article is part of a Special Issue on Spectroscopy at the University of New Brunswick in honour of Colan Linton and Ron Lees. *Canadian Journal of Physics*, **87**(May), 469–484.
- Tran, H., Turbet, M., Chelin, P., & Landsheere, X. 2018. Measurements and modeling of absorption by CO₂+ H₂O mixtures in the spectral region beyond the CO₂ ν_3 -band head. *Icarus*, **306**(May), 116–121.
- Turbet, M., Forget, F., Svetsov, V., Tran, H., Hartmann, J.-M., Karatekin, O., Gillmann, C., Popova, O., & Head, J. 2017a. The Environmental Effect of Meteoritic Impacts on Early Mars with a Versatile 3-D Global Climate Model. *LPI Contributions*, **2014**(Oct.), 3062.
- Turbet, M., Tran, H., Hartmann, J.-M., & Forget, F. 2017b. Toward a more Accurate Spectroscopy of CO₂/H₂O-Rich Atmospheres: Implications for the Early Martian Atmosphere. *LPI Contributions*, **2014**(Oct.), 3063.